JOURNAL OF MATERIALS SCIENCE 29 (1994) 3637–3642

Solidification morphology and semisolid deformation in the superalloy Rene 108

Part III *Equiaxed solidified microstructures*

C. S. LIN, J. A. SEKHAR
Department of Materials Science and Engineering, International Center for Micropyretics, University of Cincinnati, Cincinnati, OH 45221-0012, USA

A high-temperature nickel-base superalloy (Rene 108) was solidified at various cooling rates. The morphology of the equiaxed microstructure and the mechanism for intrinsic microporosity formation were correlated to the processing parameters. A special Gleeble testing procedure (developed previously – where the samples were quickly raised to a predetermined temperature in the semisolid zone and fractured) was used for the measurement of the fracture data. The upper coherent temperature was noted to be a function of the solidification variables. The amount of strain accommodation and the hot-tearing resistance was found to be influenced by the solidification microstructure. The hot ductility, the semisolid strength, and the corresponding microstructural changes are examined and discussed. Fracture maps which include the temperature, transverse-fracture stress and cooling rate during solidification (T–σ_T–$\dot{T}$) for the equiaxed solidified microstructures are presented. A castability map was created from the fracture data.

1. Introduction

The casting conditions for complex alloys, such as superalloys [1–4], influence their hot cracking and residual cracks. In nickel–base superalloys, the otherwise excellent fatigue and oxidation properties may be marred by faulty processing [5–9]. In this article, we examine the influence of the solidification morphology on the mechanical properties of the mushy zone in the nickel-base superalloy Rene 108. The processing maps for obtaining tear-free castings with equiaxed solidified structures is also discussed. A typical castability map for obtaining tear-free castings is developed for Rene 108. The type of experiments reported in this article are similar to those published previously for nickel aluminide [3, 4].

2. Experimental procedure

The normal composition of Rene 108 alloy is shown in Table I. Rene 108 alloys were equiaxed solidified in a controlled manner. The controlled equiaxed solidification system had been designed previously [10], and it consisted of a controlled solidification chamber, a Eurotherm 462 SCR and a Eurotherm 818P programmable temperature controller, see Fig. 1. A spiral–shaped SiC heating element was used as the heat source for melting. A spiral-shaped copper tube attached to a vertical alumina tube surrounded this SiC bar. Water flow in the vertical copper tube was used to cool the air-flow tube. Thin insulation wool was placed between the SiC heating element and the copper coil to prevent excessive heat being carried out by the water flow. Nozzles, along the copper tube for the air stream, were used to cool the heating element and the casting, in order to obtain high cooling rates. Constant cooling rates were obtained by programming the temperature controller at a desired value. The pieces of Rene 108 were than placed in the ceramic tube (6.0 mm inner diameter by 2.0 mm thick by 20.5 cm in height) for the process of remelting. S-type thermocouples, Pt versus Pt–10%Rh, were located 18 cm below the top of the tube as programming thermocouples, and record thermocouples were carefully positioned to touch the specimen surface. The controlled equiaxed solidification system was used to preselect different cooling rates ($0.05 \sim 12.5$ $K\,s^{-1}$) for the experiment. The as-solidified equiaxed samples were sliced, mounted and polished up to 0.03 μm grid. Cut sections of the samples were etched with a solution of 4HCL, $3HNO_3$, 2-glacial acetic acid, 1-glycerol. Information was collected from the equiaxed samples from randomly cut planes. Six photomicrographs were taken for each plane. The secondary-dendrite-arm spacing was measured at $\times 500$ for a cooling rate of $0.05\,K\,s^{-1}$, at $\times 100$ for cooling rates of 0.5 and $1.5\,K\,s^{-1}$, and at $\times 200$ for a cooling rate of $12.5\,K\,s^{-1}$. The photomicrographs were digitized by an optical scanner and then transmitted to a computer for analysis.

A hot-tension test of the as-cast alloy was conducted with a Gleeble-1500 thermomechanical simulator. This tensile test was performed to obtain the ductility and strength at elevated temperatures in the range $1362 \sim 1490$ K. The experimental details of the

0022–2461

TABLE I Composition of the alloy Rene 108

C	Si	Mn	Co	Ni	Cr	Fe	Mo	W	P
0.08	< 0.01	< 0.01	9.48	Balance	8.31	0.02	0.47	9.44	0.002
Ti	Al	Ce	Ta	V	S	Zr	Cu	Hf	Pb
0.72	5.45	< 0.01	2.99	< 0.01	0.014	0.01	0.01	1.48	< 0.1ND[a]
Ag	Tb	Tl	Mg	N	O				
< 0.1ND[a]	< 0.1ND[a]	< 0.1ND[a]	0.0008	0.0002	0.0003				

[a] ND, not detectable

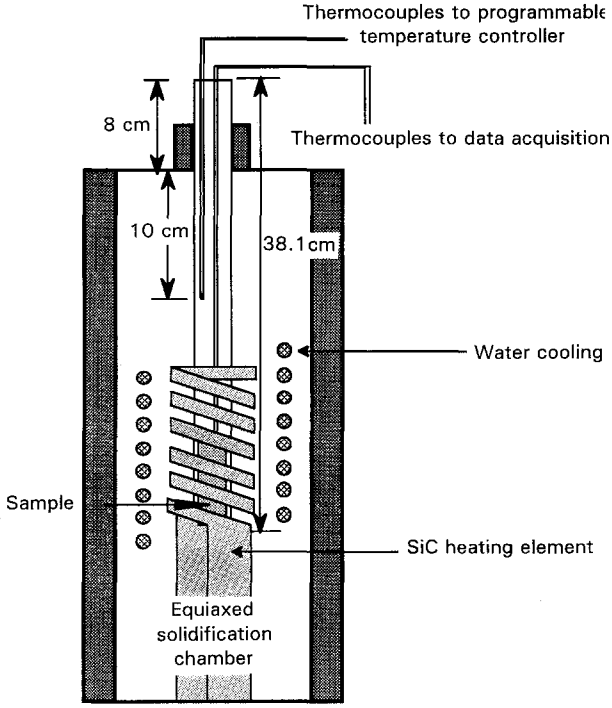

Figure 1 A schematic diagram of the equiaxed solidification system [10].

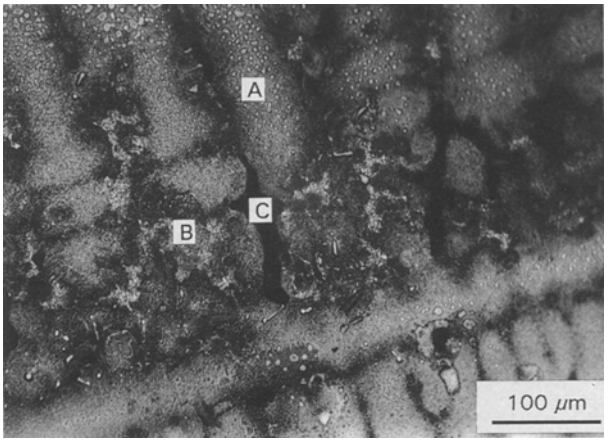

Figure 2 A typical dendrite in an equiaxed-grain microstructure for the Rene 108 alloy solidified at 1.5 K s^{-1} in air. Region A is the γ-phase dendrites. Region B is the interdendritic γ/γ′ eutectic. Region C is the porosity.

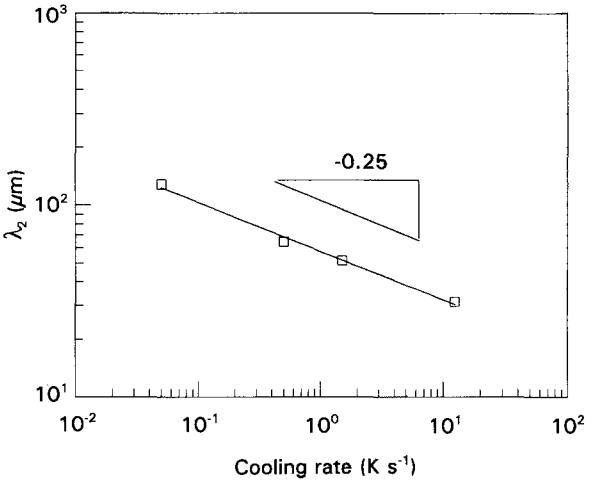

Figure 3 The correlation of the secondary-dendrite-arm spacing with the imposed cooling rate for the equiaxed solidified Rene 108 alloy.

Gleeble testing were discussed in our previous papers [3, 4]. Gleeble testing of the Rene 108 samples (with water-cooled ends for gripping) was performed at various temperatures with an argon-gas cover. The local temperature along the fracture line was measured with a 0.25 mm diameter Pt/Rh–Pt thermocouple which was spot welded to the specimen. Continuous temperature recording was made during the test. Once the specimens were ruptured, the opening of the circuit allowed the sample to cool quickly to room temperature. The fracture surfaces of the tensile-tested specimens were studied by scanning electron microscopy (SEM) to observe the fracture mode.

3. Results and discussion

3.1. Microstructure

The equiaxed microstructure of a nickel-based superalloy consisted of several randomly oriented equiaxed γ-grains. Fig. 2 shows a typical microstructure in the Rene 108 specimen solidified at 1.5 K s^{-1} in air.

The morphology of the γ-dendrites, the γ/γ′ eutectic at the interdendritic region and the γ′-cell are shown in Fig. 2. The variation in the secondary-dendrite-arm spacing, λ_2, was found to decrease with increasing imposed cooling rate, as shown in Fig. 3. For the Rene 108, the correlation of the secondary-dendrite-arm spacing, λ_2, with the imposed cooling rate may be expressed as

$$\lambda_2 = 57.43\,(dT/dt)^{-0.25}$$

where λ_2 is the secondary-dendrite-arm spacing and dT/dt is the imposed cooling rate.

3.2. Porosity and γ′-volume fraction

The solidification sequence during cooling, based on the Ni–Al phase diagram given by Verhoeven *et al.*

[11], has been previously reported for directionally and equiaxed solidified multicomponent nickel aluminide [10, 12–14]. The mechanism for microporosity formation during the equiaxed solidification process is attributed to the shrinkage of the ordered γ′-phase during liquid/solid transformation in the interdendritic region [12]. The variations in the microstructure scales of γ′ and porosity were measured and plotted against the imposed cooling rates, as shown in Fig. 4. The volume fraction of the intrinsic microporosity and the volume fraction of γ′, as a function of the imposed cooling rates, are shown in Fig. 5. The volume fraction and size of the γ′-phase particles decreased with the imposed cooling rate but the volume fraction of the porosity had its highest value for the 1.5 K s^{-1} cooling rate.

3.3. Fracture in the equiaxed solidified alloy

The stress–strain relationships for the alloy were obtained with the Gleeble at various temperatures from 1362 to 1490 K for the equiaxed solidified microstructures. For Rene 108, the solidus temperature was 1400 K and the liquidus temperature was 1769 K. A typical relationship is shown in Fig. 6. It was found that at 1470 K, or lower temperatures, a significant amount of work-hardening-type phenomena was noted; that is, the flow stress increased continuously with increasing strain. Above 1470 K, the stress curve reached a steady-state condition which was sustained even if the strain increased to 0.3 ~ 0.4. The increase in the stress from the work hardening was balanced by dynamic recovery during hot working. Therefore, the strain had little influence on the deformation resistance at temperatures above 1470 K. At the higher temperatures of 1475 and 1490 K, the 0.2% yield strength was not measurable and the ultimate tensile strength was only 3 and 2 MPa, respectively. This meant that the alloy almost lost its strength above 1490 K. This temperature is called the upper hot-tearing temperature [3, 4, 15–17]. The upper coherent temperature was noted to be a function of the imposed solidification variables, as shown in Fig. 7. As the

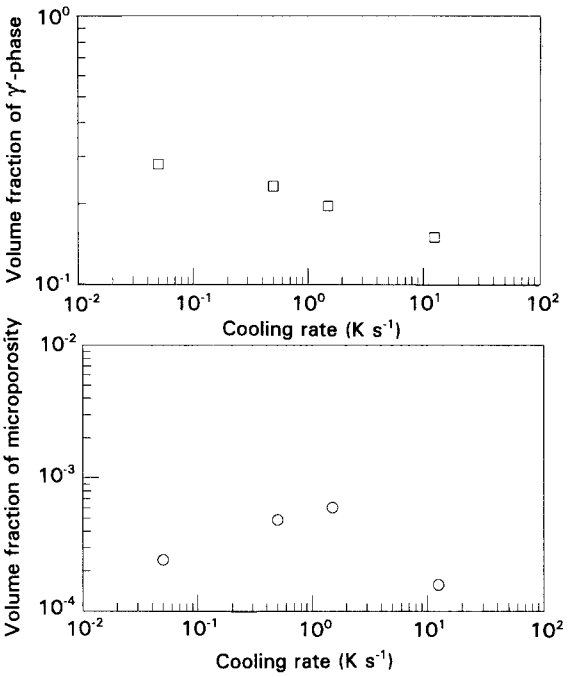

Figure 5 The volume fraction of the γ′-particles and of the microporosity in the Rene 108 nickel-base superalloy.

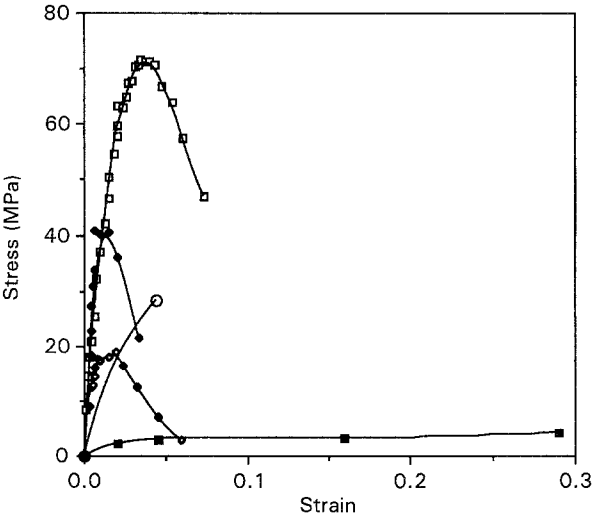

Figure 6 The stress–strain relationship for equiaxed solidified Rene 108, at a cooling rate of 0.5 K s^{-1}: (□) 1398 K, (◆) 1435 K, (○) 1444 K, (◇) 1456 K, and (■) 1475 K.

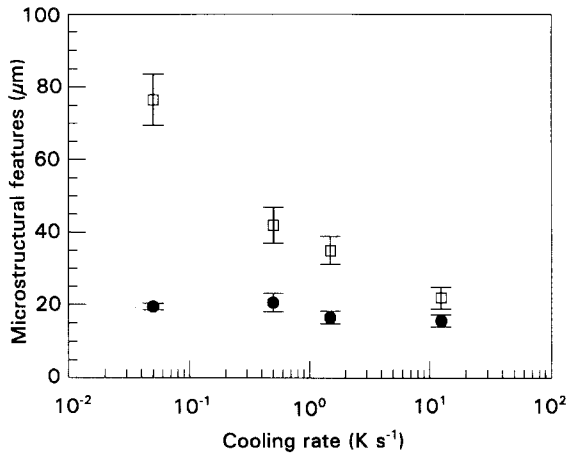

Figure 4 The variation of the mean radius of (□) the γ′-particles and (●) the porosity with the imposed cooling rate for the Rene 108 alloy.

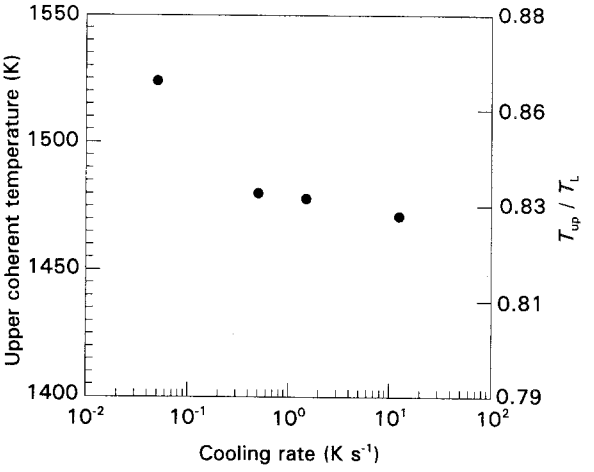

Figure 7 The upper coherent temperature/liquid temperature, T_{up}/T_L, versus the cooling rate for the equiaxed solidified Rene 108.

cooling rate increased, the stress to fracture increased at a given temperature, as shown in Fig. 8. Similarly, the upper coherent temperature increased with decreasing cooling rate. At the higher cooling rates, fine secondary-arm spacings and smaller grains were noted. As a result, a larger grain-boundary area was obtained. At high temperatures (> 1450 K), the grain boundaries were weak, especially in the presence of a liquid film. Therefore, the samples cooled at high cooling rates, which had large grain-boundary areas, had low fracture stresses at high temperatures and higher fracture stresses at low temperatures. Table II shows the modulus measured as a function of the temperature and the solidification variables for the samples tested in this study.

3.4. Hot-tearing susceptibility

The hot ductility of the nickel-base superalloy as a function of temperature is shown in Fig. 9. The trend for all the materials was that the hot ductility increased with decreasing testing temperature (from zero to peak ductility) and then decreased slowly. Ductility minima of a kind reported in [3, 4] were also observed. The temperature of the peaks and minima were noted to be a function of the cooling rate.

The reason for the low ductility at high temperatures and again at the low temperatures can be explained by considering the sample solidified at 12.5 K s^{-1}. At the temperature of 1453 K, a few discontinuously precipitated interdendritic phases were observed with small cracks propagating along them, shown in Fig. 10. Intergranular cracking was noted, in Fig. 10, to be the predominant feature at this temperature; this accounted for the drop-off in ductility. At a temperature of 1470 K, a liquid interdendritic phase occurred continuously along the grain boundary, and incipient melting was evident; see Fig. 11. The poor ductility obtained at 1470 K was thus related to the incipient melting of the grain boundary. Microstructural evidence of incipient melting at high temperature has also been observed for cobalt-base superalloys and nickel aluminides [3, 4, 9], corresponding to such embrittlement at elevated temperatures.

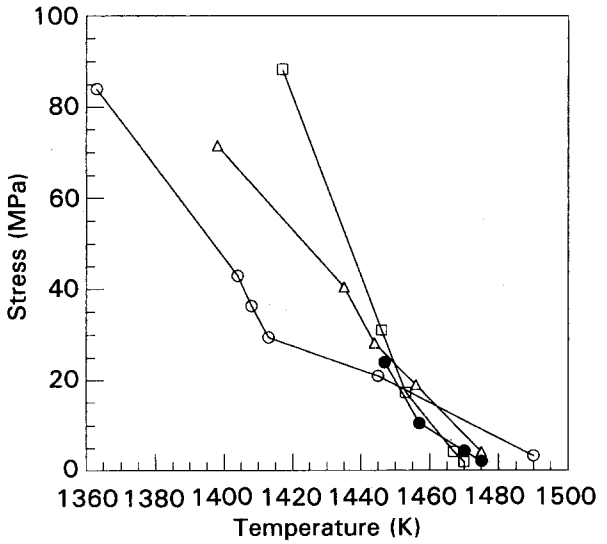

Figure 8 The stress at failure versus the temperature for equiaxed solidified Rene 108 for the following cooling rates during solidification: (○) 0.05 K s^{-1}, (△) 0.5 K s^{-1}, (●) 1.5 K s^{-1}, and (□) 12.5 K s^{-1}.

TABLE II Measured mushy-zone properties from stress-free equiaxed solidified Rene 108

Cooling rate (K s^{-1})	Temperature (K)	E_T (MPa)	σ_f (MPa)	$\alpha E_T(T_L - T)/\sigma_f$
12.5	1417	1225	88.4	0.066338
12.5	1446	3935	31.09	0.55599
12.5	1453	914	17.36	0.22627
12.5	1467	52	4.25	0.050253
12.5	1470	191	1.91	0.40664
1.5	1447	3405	24.03	0.62052
1.5	1457	1509	10.56	0.60634
1.5	1470	1095	4.38	1.0166
1.5	1475	63	2.06	0.12228
0.5	1398	7260	71.52	0.51218
0.5	1435	4541	40.7	0.50681
0.5	1444	641	28.22	0.1004
0.5	1456	1333	19	0.29865
0.5	1475	83	3.25	0.10211
0.05	1363	4952	84.036	0.32537
0.05	1404	2775	42.897	0.32112
0.05	1408	2591	36.301	0.35042
0.05	1413	1983	29.46	0.3259
0.05	1445	1233	20.967	0.25913
0.05	1490	96	3.25	0.11208

α was taken to be 13.6×10^{-6} K^{-1} for the alloy. E_T is the modulus measured at a given temperature. T_L is the liquidus temperature. T is a given temperature. σ_f is the fracture stress at the same temperature. The modulus E_T is determined from the average slope between the first two or three data points of the type shown in Fig. 6. This modulus may somewhat underestimate the slope at the origin.

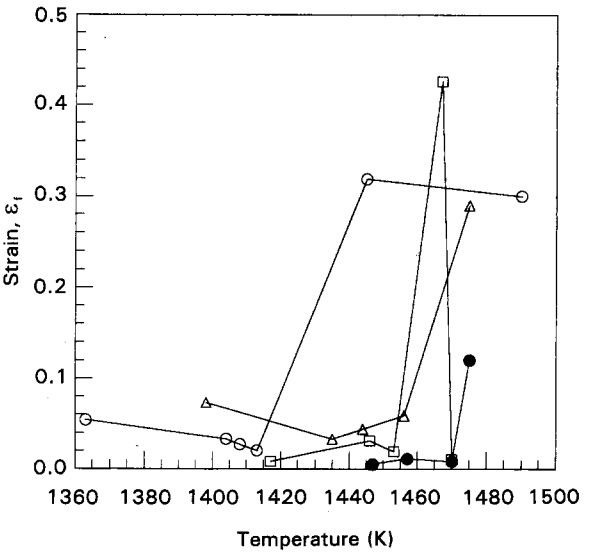

Figure 9 The strain at failure ε_f, versus temperature for the equiaxed solidified Rene 108. For key, see Fig. 8.

Fig. 12 shows fracture surface of the alloy cooled at 0.05 K s^{-1}. The sample with high ductility (T = 1463 K) showed many dimples; this indicated that the hot ductility had been improved significantly. At this temperature, the grain-boundary film was thinner than was required for efficient crack propagation, yet

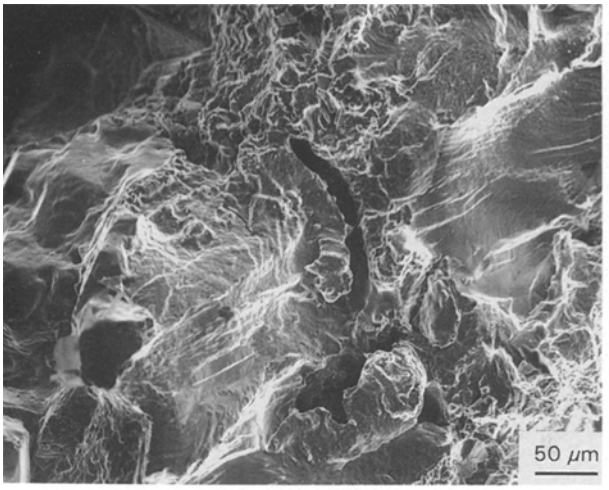

Figure 10 A SEM micrograph of the fracture surface of the equiaxed solidified Rene 108 Ni-base superalloy after a tensile test at 1453 K. The cooling rate imposed during solidification was 12.5 K s^{-1}.

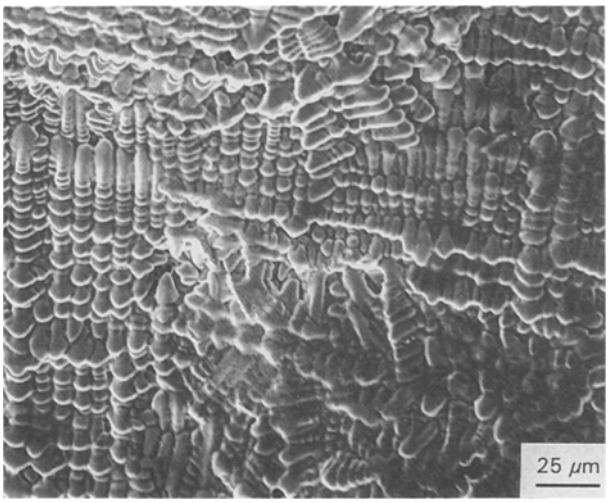

Figure 11 A SEM micrograph of the fracture surface of the equiaxed solidified Rene 108 Ni–base superalloy after a tensile test at 1470 K. The cooling rate imposed during solidification was 12.5 K s^{-1}.

strain accommodation was possible. At temperatures higher than this, the film was too thick. At lower temperatures, cracking could occur but no sliding was possible for strain accommodation. Thus, good ductility was possible where strain accommodation was possible without the possibility of efficient crack propagation. The temperature for this high ductility was related to the microsegregation and thus it was different for different cooling rates.

3.5. Fracture maps and castability maps for equiaxed solidified nickel-base superalloy Rene 108

The castability concept has been discussed in [18] and castability maps for multicomponent nickel aluminide [3, 4] have been generated in previous studies. Similar fracture maps and castability maps for equiaxed solidified nickel-base superalloy Rene 108 are shown in

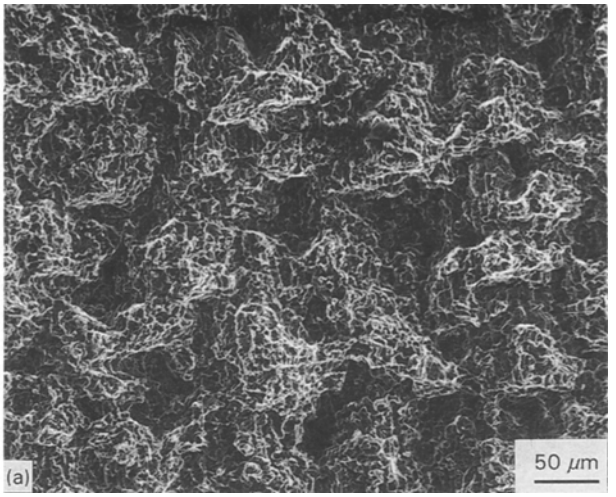

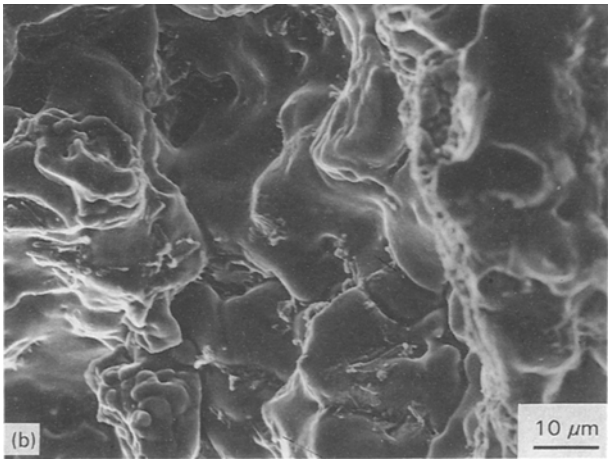

Figure 12 Typical fracture surfaces of the equiaxed solidified Rene 108 (at a cooling rate of 0.05 K s^{-1}) observed by SEM: (a) tested at 1365 K, and (b) tested at 1490 K.

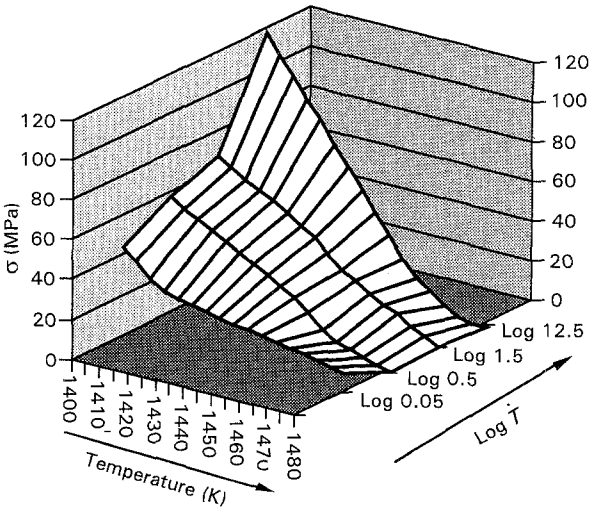

Figure 13 A three dimensional diagram fracture map (stress at fracture versus temperature versus cooling rate) for the equiaxed solidified Rene 108 alloy.

Figs 13 and 14. These maps reflect the conditions under which the casting will tear during processing. The fracture map for Rene 108 was developed after a critical examination of the solidified microstructure and the semisolid strengths. The fracture map is a

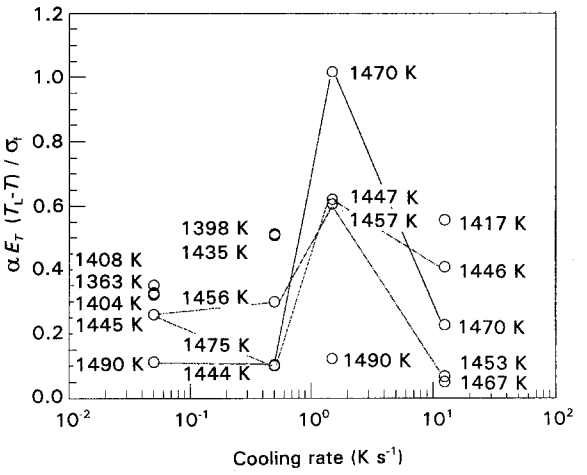

Figure 14 The ratio of imposed stress to the fracture stress at a given temperature versus the cooling rate for Rene 108. α was taken to be $13.6 \times 10^{-6} K^{-1}$ for the alloy. E_T is the modulus measured at a given temperature. T_L is the liquidus temperature. T is a given temperature. σ_f is the fracture stress at the same temperature. This is the equiaxed solidified castability map for the Rene 108 alloy.

graph of σ_f versus T versus $\dot{T}$ (that is, the fracture stress, the temperature and the cooling rate) for the equiaxed microstructure. This is shown in Fig. 13. The most important processing variable in the equiaxed casting is the cooling rate, $\dot{T}$. Fig. 14 shows a plot of the ratio of imposed stress to the fracture stress, at a given temperature, as a function of cooling rate. Note that the imposed stresses approach the fracture stress values at an intermediate cooling rate; this cooling rate should be avoided during the processing of Rene 108 castings. (See [18] for a discussion of such graphs on processing.) Table II shows the measured mechanical properties of the superalloy Rene 108. This data was used to produce Fig. 14. The thermal-expansion coefficient α, was taken to be $13.6 \times 10^{-6} K^{-1}$ for the alloy, σ_f is the fracture stress at a given temperature, T, and E_T is the modulus measured at the same temperature. The quantities σ_f and E_T are measured from plots such as those in Fig. 6.

4. Conclusions

A study of the solidification crack susceptibility of a nickel-base superalloy was performed using a Gleeble 1500 simulator. The hot tensile properties and microstructures of an as-cast nickel-base superalloy were studied in the range 1362–1490 K. The main results were as follows.

1. For the equiaxed microstructure, the volume fraction of the intrinsic porosity was a function of cooling rate. The size of the porosity showed a decreasing tendency with increasing cooling rate. The mechanism for microporosity formation during the equiaxed solidification process is attributable to the shrinkage of the ordered γ'-phase during liquid-/solid transformation in the interdendritic region.

2. The upper hot-tearing temperatures and the temperature of the maximum and minimum ductility were functions of the imposed solidification variables.

3. The fracture map T–σ_f–$\dot{T}$ may be used for the design of castings. The solidification and cooling rates selected for this study lay in the range of cooling rates commonly employed for commercial casting purposes. For a casting process, we may obtain information on the cooling rate during solidification. In addition, it is fairly simple to estimate the magnitude of mould-imposed stress on a casting [19–22]. By comparing the values with the T–σ_f–$\dot{T}$ plot, it may be determined if there is any value that lies above the net. If a problem is anticipated, parameters like the mould design, the cooling rate, etc., may be changed to ascertain that there is no processing condition above the critical net.

4. Castability maps indicate that the susceptibility to cracking is greatest at intermediate cooling rates ($\sim 1.5 K s^{-1}$).

Acknowledgements

This work was performed as a part of an Edison Material Technology project CT-17.

References

1. Y. F. GUVEN and J. D. HUNT, *Cast Metals* **1** (1988), 104.
2. J. CAMPBELL and T. W. CLYNE, *ibid.* **3** (1991) 224.
3. C. S. LIN and J. A. SEKHAR, *J. Mater. Sci.* **28** (1993) 3581.
4. *Idem., ibid.* **28** (1993) 3885.
5. J. K. TIEN, G. E. VIGNOUL and M. W. KOPP, *Mater. Sci. Engng. A* **143** (1991) 43.
6. V. K. SIKKA, J. T. MAVITY and K. ANDERSON *ibid. A* **153** (1992) 712.
7. J. E. DOHERTY, B. H. KEAR and A. F. GIAMEI, *J. Met.* **11** (1971) 59.
8. F. H. FROES, *ibid.* **9** (1989) 6.
9. J. C. TSAI and J. B. DUH, *Scripta Metall.* **27** (1992) 561.
10. C. J. CHENG, PhD Thesis University of Cincinnati, Cincinnati, (1992).
11. J. D. VERHOEVEN, J. H. LEE, F. C. LAABS and L. L. JONES, *J. of Phase Equilibria*, in press.
12. C. J. CHENG and J. A. SEKHAR, Materials Research Society Conference Proceedings on High Temperature Ordered Intermetallic Alloys IV, edited by L. A. Johnson, D. P. Pope and J. O. Stiegler (Materials Research Society, Pittsburgh, 1991) p. 853.
13. C. T. HO, C. J. CHENG and J. A. SEKHAR, *Metall. Trans., A* **22** (1991) 225.
14. C. J. CHENG and J. A. SEKHAR, Solidification Microporosity in IC 396M: Nickel Aluminide Vol. 2, Final Report, Equiaxed Solidification (Oak Ridge National Laboratory, Oak Ridge, 1990).
15. J. C. BORLAND, *Brit. Weld J.* **7** (1969) 508.
16. *Idem, Welding and Metal Fabrication*, January/February (1979) 19.
17. *Idem., ibid.* March (1979) 99.
18. J. A. SEKHAR, C. S. LIN and C. J. CHENG, "Nature and properties of semi-solid materials", edited by J. A. Sekhar and J. Dantzig (The Minerals, Metals and Materials Society, Warrendale, PA, 1991) 267.
19. M. C. FLEMINGS, "Solidification processing" (McGraw-Hill, New York 1974).
20. A. ETIENNE and A. PALMERS, "Solidification and casting of metal" (The Metals Society, London 1979) 295.
21. A. GRILL, J. K. BRIMACOMBE and F. WEINBERG, *J.I.S.I.* **211** (1976) 34.
22. J. MATHEW and H. D. BRODY, "Solidification and casting of metal" (The Metals Society, London, 1979) p. 244.

Received 15 December 1993
and accepted 10 January 1994